Collapsed carbon nanotubes as building blocks for high-performance thermal materials

Jihong Al-Ghalith,[1] Hao Xu,[2] and Traian Dumitrică[1,2,*]

[1]*Department of Mechanical Engineering, University of Minnesota, Twin Cities, Minnesota 55455, USA*

[2]*Department of Aerospace Engineering and Mechanics, University of Minnesota, Twin Cities, Minnesota 55455, USA*

(Received 11 July 2017; revised manuscript received 29 September 2017; published 25 October 2017)

The influence of collapsed shape on the thermal transport of carbon nanotubes is studied by nonequilibrium molecular dynamics. Nanotubes of different lengths, diameters, chiralities, and degrees of twist are simulated in the regime in which the thermal transport extends from ballistic to diffusive. In contrast with graphene nanoribbons, which are known to exhibit substantial rough-edge and cross-plain phonon scatterings, the collapsed tubes preserve the quasiballistic phononic transport encountered in cylindrical nanotubes. Stacked-collapsed nanotube architectures, closely related with the strain-induced aligned tubes occurring in stretched nanotube sheets, are shown to inherit the ultrahigh thermal conductivities of individual tubes, and are therefore proposed to form highways for efficient heat transport in lightweight composite materials.

DOI: 10.1103/PhysRevMaterials.1.056001

I. INTRODUCTION

The continuous advances in carbon nanotube (CNT) processing technology have brought about a new class of synthetic materials, which include large-volume CNT sheets suitable for developing macroscale applications [1]. The sheet exhibits a network structure comprising partially aligned and highly entangled millimeter-long CNTs, which gives rise to a large variety of physical properties [2,3]. Currently, there are significant efforts to manipulate CNT orientation [4] in order to control macroscale properties and impart the network the exceptional mechanical, thermal, and electrical attributes of individual CNTs [5,6]. For example, by mechanically stretching CNT sheets [4], a 22-fold improvement in the Young's modulus and a 44% increase in electrical conductivity along the stretch direction have been reported [7]. Interestingly, recent atomic-resolution transmission electron microscopy analysis of the stretched-processed sheets [8] found massive presence of long, flattened CNTs [9]. Thus, during sheet stretching, the initially cylindrical large-diameter CNTs undergo not only alignments but also permanent radial collapse to a dog-bone-shaped cross section.

The thermal properties of CNTs are of significant interest since the thermal conductivity (κ) of suspended single-walled cylindrical CNTs—1500–3500 $\mathrm{W\,m^{-1}\,K^{-1}}$ at room temperature [6,10,11]—is comparable with the in-plane κ of graphite and diamond, which are among the best known thermal conducting materials. Molecular dynamics (MD) simulations showed that defects in CNTs, including bends and kinks, could significantly reduce κ as they strongly suppress high-frequency phonon modes [12]. Although the existence of collapsed CNTs has been known for decades [13], and their energetic stability, mechanical, and electronic properties are well understood [14–16], thermal transport along these nanostructures has received less attention. The impact on κ of the CNT circumference collapse, in which opposite faces form a van der Waals (vdW) bilayer with two nearly circular edges, Fig. 1(a), is not known. This is a valid problem, since edges [17,18] and cross-layer scattering [19,20] can drastically impact the heat carrying abilities of graphitic materials. Additionally, collapsed CNTs are very susceptible to torsional deformations [16,21], which might also affect κ.

By way of nonequilibrium MD simulations carried out with LAMMPS [22], here we examine phononic transport, which is expected to be the dominant component of the thermal transport in both metallic and semiconducting CNTs [11]. We consider not only individual CNT structures, Fig. 1(a), but also tightly packed collapsed CNT systems, Fig. 1(b), to probe the robustness of the thermal transport to the potential quenching of the heat-carrying phonon modes by neighboring CNTs. To this end, we investigated various morphologies, including isolated collapsed single-walled CNTs, and experimentally relevant [9] collapsed CNT stacks. To probe the edge, layer coupling, width, chirality, twist, and the number-of-tubes structural effects, as well as the CNTs length scales needed to cover both the ballistic and diffusive transport, we simulated systems containing up to 1 228 800 carbon atoms.

II. COMPUTATIONAL METHODS

To prepare the collapsed CNTs, a Nose-Hoover thermostat was used initially to equilibrate the cylindrical CNTs at 5 K. After the system reached equilibrium, a 0.01 eV/Å force was added in the transverse direction for 15 ps to squeeze the structure. The system was then freed in the transverse direction and equilibrated again under microcanonical ensemble for another 500 ps. Periodic boundary conditions were applied in the axial direction throughout the whole process. In the end, we used conjugate gradient relaxation to relax the collapsed structures at 0 K. The structures remained collapsed during the subsequent MD studies. The twisted collapsed CNTs were created by performing structural relaxations under objective boundary conditions [23]. The packed collapsed CNTs were created via relaxations under triclinic periodic boundary conditions.

The geometry of the collapsed CNTs balances the bending energy stored in the bulging, nearly circularizing edges with the vdW energy gained from drawing the flattened CNT walls close together. Thus, the interatomic forces play a dominant role in establishing the shapes of the collapsed CNTs. The selection of the interatomic classical potential is particularly

*Corresponding author: dtraian@umn.edu

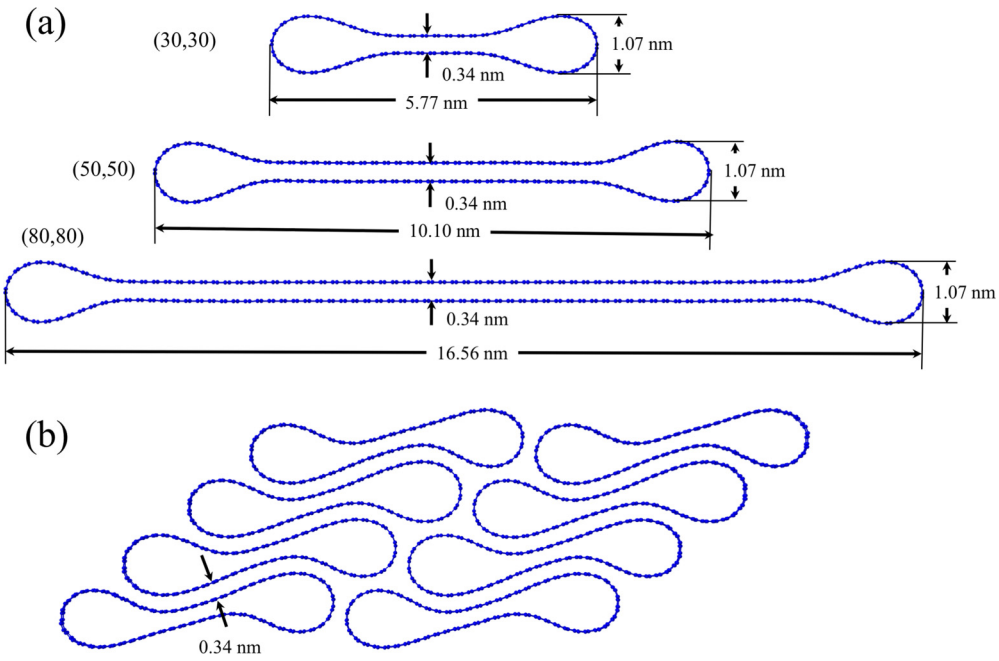

FIG. 1. Cross section of the optimized (a) collapsed (30,30), (50,50), and (80,80) CNTs (from top to bottom), and (b) stacked collapsed (30,30) CNTs.

subtle as the molecular mechanics of the available bond-order potentials with vdW interactions—AIREBO [24] and REBO [25]—describe bending strain differently [26]. In this respect, Fig. 2 shows that the nearly circular edges of the collapsed single-walled CNTs present different diameters, even when the same Lennard-Jones (L-J) parameters (energy parameter $\varepsilon = 2.84$ meV and the distance parameter $\sigma = 3.4$ Å) are used to describe the vdW interactions. We selected the Tersoff potential [27] for our calculations, which was optimized to produce a phonon dispersion for the heat carrying phonon modes of CNTs and graphene in good agreement with experimental evidence [28]. To describe the collapsed CNTs, we have further added L-J interactions between the C-C atoms located on opposite faces with L-J parameters ($\varepsilon = 3.5$ meV and $\sigma = 3.4$ Å) adjusted to describe stress-free collapsed geometries similar to those obtained with accurate force fields derived from *ab initio* calculations and experiments [14,15].

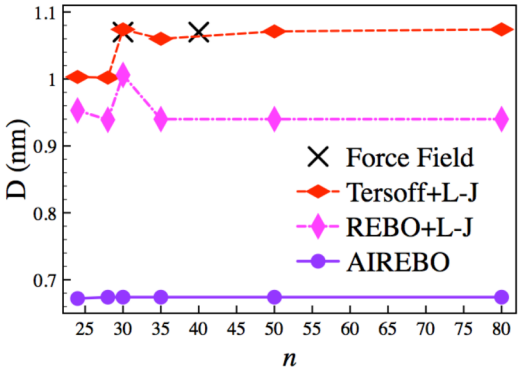

FIG. 2. Diameter (D) of the nearly circular edges of (n, n) CNTs versus n, as calculated with several bond-order potentials. The force-field data are taken from Ref. [15].

The setup used for the κ calculations is described in Figs. 3(a) and 3(b). A one-unit cell ring at each end of the tube was kept fixed throughout the simulation to prevent the center of the mass of the system from moving, and to impose a torsional deformation. Four other neighboring unit cells were designated as "hot" and "cold" baths. In selecting a simulation setup with relatively small bath regions, we have followed the guidelines of Salaway and Zhigilei [29], which emerged from systematic length-dependent convergence studies of κ performed in cylindrical CNTs. We have also adopted their notion that κ reflects not only the thermal behavior of the CNT portion located between the bath regions, but also of the bath regions themselves. In this respect, our tests on large-diameter collapsed CNTs with different sizes of bath region produced stable thermal conductivities in different CNT length regimes, see Fig. S1 in the Supplemental Material [30]. Therefore, in our subsequent κ vs length plots, we have used the CNT length with the bath regions included.

In preparation for the thermal calculations, the system was initially equilibrated at 300 K with a Nose-Hoover thermostat after which the two reservoirs were rescaled at every time step to maintain $T_h = 310$ K and $T_c = 290$ K, respectively. Under velocity Verlet cycling with a 0.5 fs time step, a steady state was reached after 1000 ps or longer, depending on the sample length. The collapsed CNT shape without any edge breaking was maintained throughout the MD simulation, Fig. S2 [30]. The heat flux along CNTs was obtained by calculating the difference of the rate of the kinetic energy extraction from the two reservoirs $\dot{Q} = 0.5\langle \dot{Q}_h - \dot{Q}_c \rangle$, where $\dot{Q}_h$ and $\dot{Q}_c$ are the instantaneous heat currents flowing into and away from the hot and cold baths to maintain the temperature gradient, Fig. 3(c). The angular brackets indicate a statistical average taken after the steady state was reached. From the dependence of the local temperature T, obtained here by statistically averaging the kinetic energy of the atoms located in one unit

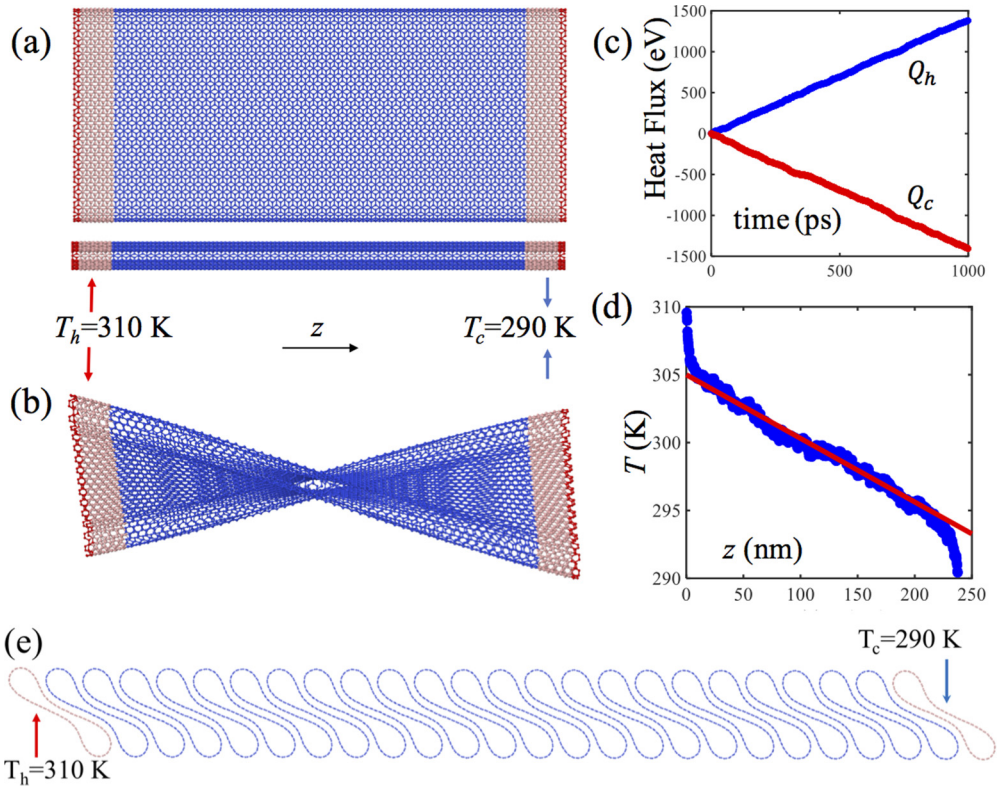

FIG. 3. Nonequilibrium MD setup for (a) straight and (b) twisted collapsed (30,30) CNTs. The twist rate is 0.105 rad/nm. (c) Temperature (blue circles) profiles in a straight (30,30) CNTs 250 nm in length. The fitted line is shown in red. (d) The heat fluxes flowing into the hot Q_h and cold reservoir Q_c at the steady state. (e) Nonequilibrium MD setup for computing the intertube thermal resistance R in a stack of 23 collapsed (30,30) CNTs.

cell, on the axial position z, we obtained the temperature profile shown in Fig. 3(d). To minimize the effects of fluctuations in local T, the κ presented in each figure is the average of five data sets taken after reaching the steady state. Accordingly, the error bars in each figure represent the standard deviation. κ is calculated with Fourier's law $\kappa = -\dot{q}(dT/dz)^{-1}$. Here $\dot{q}$ is $\dot{Q}$ per cross-sectional area, which is defined here by the thickness of the single atomic layer in a tube wall, 0.34 nm, multiplied by the circumference of the cylindrical CNT. For collapsed CNTs, the inextensible deformation approximation is justified in view of the large width of the bilayer region and the nanometer-scale diameter of the nearly circular edges [26]. Therefore, the cross-sectional area of collapsed CNTs is taken to be the same as that of the original cylindrical CNT. Any potential changes in κ under circumferential collapse reported next cannot be attributed to different definitions of the cross-sectional area.

For the calculations of the interfacial thermal resistance R between collapsed (30,30) CNTs, heat baths were applied on the left and right CNTs of the stack, as shown in Fig. 3(e). The CNTs between the two heat baths are free to move. R between tubes is calculated from $(N-1)R = L/\kappa_i$, where κ_i is the computed thermal conductivity in the interfacial direction (y direction), L and N are the total between-bath distance and the number of CNTs between the two heat baths, respectively. The contact area is 18.7 nm^2, as approximated by the width of the collapsed CNT in vdW contact of 5 nm times the PBC length in the z direction.

III. RESULTS AND DISCUSSION

A. Thermal transport in individual CNTs

Before discussing the impact of the collapsed shape, it is important to first review the behavior of thermal transport in cylindrical CNTs. It is known that CNTs exhibit strong ballistic behavior over submicron length scales [31–34]. Figures 4(a) and 4(b) show that the sample length l of both (30,30) and (50,0) CNTs strongly influences κ. The initial linear increase of $\kappa \propto l$ is a signature of pure ballistic behavior, i.e., phonons are able to propagate without being scattered by the sample. As the sample length increases, more phonon modes with longer wavelengths are being supported. These modes were shown to contribute actively to an increase of κ [32], although in a nonlinear way. Another important feature is the significantly lower rate $\kappa \propto l^{0.2}$ of increase at sample lengths above ~200 nm, which signals that the thermal transport extends into the diffusive regime. κ shows signs of saturations at above ~600 nm and the slow increase exhibited beyond this length is expected to continue over micron length scales [31–34]. Figures 4(a) and 4(b) also show that the three considered interatomic potentials produce similar trends but very different κ magnitudes. To rationalize this result, we recall that the phonon dispersion plays an important role in thermal transport. While the reoptimized Tersoff potential [28] captures the quadratic behavior of the lowest frequency phonon modes near the Γ point, the REBO [25] and AIREBO [24] potentials produce linear behaviors in this region, Fig. S2

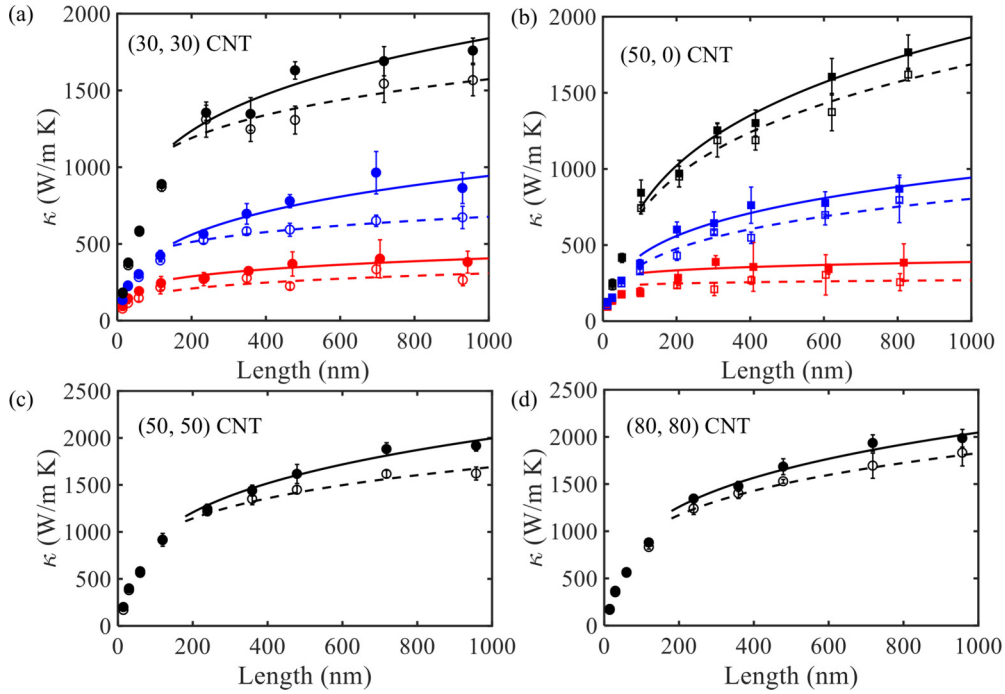

FIG. 4. κ of cylindrical (filled symbols) and collapsed (empty symbols,) (a) (30,30) CNTs (cross sectional area 4.39 nm^2), (b) (50,0) CNTs (cross sectional area 4.23 nm^2), (c) (50, 50) CNTs (cross sectional area 7.31 nm^2), and (d) (80, 80) CNTs (cross sectional area 11.70 nm^2) with different tube lengths, as calculated with reoptimized Tersoff (black), REBO (blue), and AIREBO (red) interatomic potentials. The regime in which κ extends from ballistic to diffusive is fitted as $\kappa \propto l^{0.2}$ for both cylindrical (solid line) and collapsed (dashed line) CNTs.

[30]. This artifact causes significant error in κ, specifically a 50%–80% underestimation of κ by the REBO and AIREBO when compared to the reoptimized Tersoff potential result. It is worth noting that for the longest considered cylindrical CNTs, the κ produced by the reoptimized Tersoff potential of 1600–2000 $W\,m^{-1}\,K^{-1}$, is consistent with experimental measurements [10]. In the following, we will rely on the predictions produced by this validated potential. Finally, we note that in Fig. 4, the weak dependence of κ on CNT diameter and chirality is in agreement with previous literature [31].

Figures 4(a) and 4(b) further reveal the impact on κ of the collapsed shape. In contrast with the behavior reported earlier in the bending-kink case [12], the ballistic transport is not affected by the formation of the nearly circular edges. As transport evolves into the diffusive regime, a more significant κ reduction develops, suggesting that the heat carrying phonons scatter more effectively than in the cylindrical case. In the reoptimized Tersoff potential description, we measured only an 11% κ reduction for the (30,30) collapsed CNTs at the largest length considered. The REBO and AIREBO potentials produce more substantial reductions, 22% and 31%, respectively, a trend that correlates with the diameter decrease of the nearly circular edges described by these potentials, Fig. 2. Figures 4(c) and 4(d) show a similar behavior in larger diameter armchair CNTs. Since the diameters of the nearly circular edges are the same in the shown collapsed (50, 50) and (80, 80) CNTs (see Fig. 2), the similar level of reduction in κ obtained in the wider collapsed CNTs suggest that the bilayer vdW scattering is affecting κ to a lesser extent.

It is useful to recall that MD captures naturally anharmonic effects and various scattering mechanisms. Thus, the MD-computed κ reflects both phonon dispersion effects and the phonon relaxation times (τ_Z). A CNT presents four acoustic phonon branches: two radial-breathing transverse acoustic (ZA) (atomic movement perpendicular to the CNT axis), one twist (TA) (torsional movement around the axis), and one longitudinal (LA) branch (atomic movement along the axis). For large diameter cylindrical CNTs, the dispersion curves of these acoustic modes show very little deviation from the corresponding acoustic modes of graphene [31].

Phonon dispersion modifications could be expected when changes in the mechanical properties of a monolayer occur [35]. However, the elastic properties of collapsed CNTs closely resemble those of their cylindrical counterparts. For example, MD simulations showed that stretching and compressing cylindrical and collapsed CNTs leads to overlapping strain energy curves [15]. Corroborating this observation, here we find that the phonon dispersion and phonon density of states are affected in a minor fashion by the collapsed shape, Figs. S3, S4, and S5 [30].

We have also performed a phonon spectral analysis [30,36,37] based on the MD trajectories in order to illustrate how the τ_Z of heat carrying modes are impacted by the cross-sectional collapse. In Table I we compare the calculated averaged lifetimes τ_Z of the ZA and TA phonon modes of a cylindrical and collapsed (80,80) CNTs at three selected wave vectors and frequency intervals. The reported values have a maximum of 11% uncertainty. It is noteworthy that the low-frequency ZA modes are especially important due to their significant contribution to the κ of larger diameter

TABLE I. Reoptimized Tersoff potential calculations. Comparison of τ_Z in cylindrical and collapsed (80,80) CNTs. The wave vector (units of $2\pi/a_z$, $a_z = 0.246$ nm). Each shown frequency ranges contain three phonon peaks. The lifetimes are listed in the order set by the magnitude of their frequency.

CNT shape	Wave vector ($2\pi/a_z$)	Freq. (THz)	τ_Z ZA (ps)	Freq. (THz)	τ_Z TA (ps)
Cylindrical					
	0.48	2.9–4.4	50.0; 38.5; 41.7	12.8–16.0	23.8; 22.7; 22.8
	0.60	4.8–6.2	50.0; 62.5; 41.7	16.7–18.9	23.8; 20.8; 22.7
	0.72	6.4–8.4	55.6; 50.0; 62.5	19.2–22.6	27.8; 25.0; 31.2
Collapsed					
	0.48	2.9–4.4	41.7; 20.0; 16.7	12.8–16.0	23.8; 20.0; 22.7
Edges	0.60	4.8–6.2	16.7; 35.7; 26.3	16.7–18.9	15.6; 20.8; 22.7
	0.72	6.4–8.4	25.0; 41.7; 33.3	19.2–22.6	20.0; 20.8; 22.7
	0.48	2.9–4.4	41.7; 38.5; 35.7	12.8–16.0	22.7; 20.0; 17.9
Bilayer	0.60	4.8–6.2	50.0; 55.6; 31.3	16.7–18.9	21.7; 20.8; 22.7
	0.72	6.4–8.4	55.6; 50.0; 55.6	19.2–22.6	25.0; 25.7; 27.8

cylindrical CNTs [31]. When measured in the edge region of the collapsed CNT, we see that the τ_Z values of the ZA branch are reduced significant (up a factor of 3) at most frequency peaks. In contrast, the reduction of τ_Z in the bilayer region is rather small. At the same time, the TA data (last column of Table I) also indicates that τ_Z is negligibly impacted by the edge and bi-layer regions.

In view of the minor changes in phonon dispersion, the above sampling of the lifetimes provides evidence that the small reduction in κ resulting from the cross-sectional collapse is fostered by the double role played by the nearly circular edges: (i) to increase in a gentle way the important ZA phonon scattering through the anharmonicity caused by the curvature strain [26] at the edges, and (ii) to "connect" the bilayer region in a way that limits the cross-plane scattering typical of unconnected graphene layers. By limiting cross-plane scattering, the collapsed CNTs can maintain large phonon lifetimes for the in-plane conduction modes, especially for the low frequency ZA modes.

We further emphasize that the high κ of the collapsed CNTs is unusual given the fact that phonon propagation in atomically thin graphene nanoribbons (GNRs) is especially sensitive to edge perturbation. As an example, Fig. 5(a) compares the κ of collapsed (30,30) CNTs with that of bilayer GNRs with similar widths but rough and open edges. (The rough open edges were created by opening the collapsed CNT and further eliminating atoms in a systematic manner while keeping the coordination number to at least two for the edge carbon atoms.) In contrast to the behavior of collapsed CNTs, the GNRs display diffusive phonon scattering and are not able to preserve the quasiballistic phononic transport. The longest GNR considered displays an approximately 83% reduction in κ. We note that the final $\kappa = 270\,\mathrm{W\,m^{-1}\,K^{-1}}$ computed value is consistent with experimental measurements [17,18].

Contrasting with the results obtained so far, Fig. 5(b) shows that a gradually applied twist deformation can reduce κ especially when the atomic-scale twist angle is very large. To explain this behavior, we ruled out potential changes in phonon scatterings of the nearly circular or bilayer regions since the curvature at the edges and interlayer separation do not change significantly with twist [16]. Instead, we recall that the twisted collapsed CNTs store shear strain [16]. We propose that the mechanism for enhancing phonon-phonon scattering is the anharmonicity in the interatomic potential created by the displacement of atoms from their equilibrium positions.

B. Thermal transport in stacks of collapsed CNTs

Collapsed CNTs are potentially attractive building blocks for forming mesoscale structures. Elliot *et al.* [14] investigated herringbone arrangements of collapsed single-walled CNT bundles emerging under hydrostatic pressures. Inspired by the outcomes of recent experiments in stretching induced alignment of CNT sheets [9], here we investigate tightly packed single-walled CNT architectures targeting ultrahigh κ at the

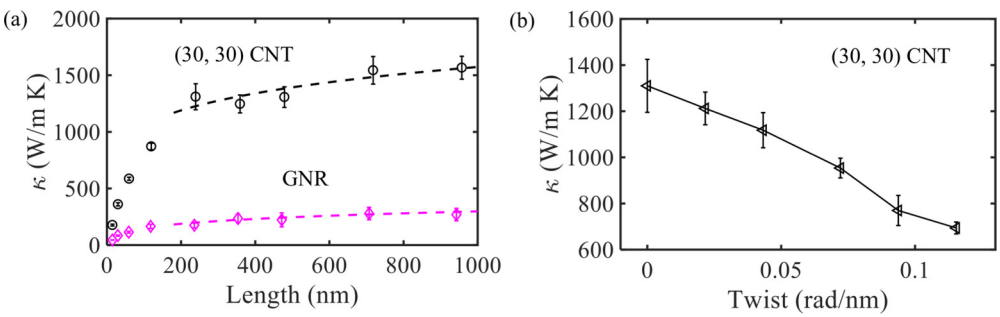

FIG. 5. (a) Comparison of κ in collapsed (30,30) CNT and two-layer GNR with similar width but rough edges. (b) κ vs twist rate in a collapsed (30,30) CNT measuring 239.33 nm. Data are from the reoptimized Tersoff potential.

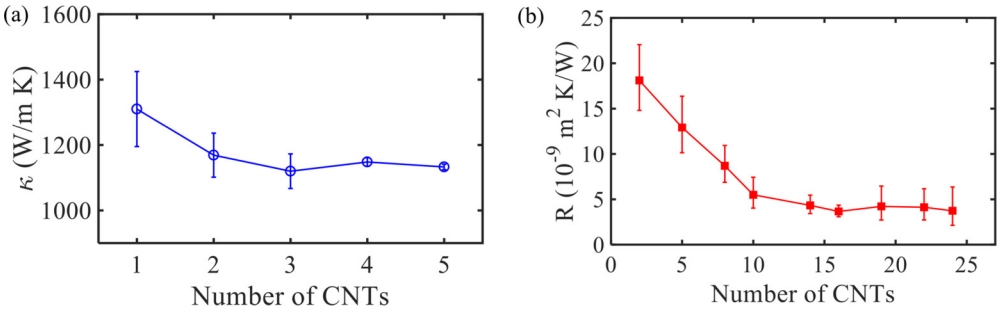

FIG. 6. (a) κ of stacked-collapsed (30,30) CNTs. The length of each CNT is 239.33 nm. (c) R across the stacked collapsed (30,30) CNTs vs the number of CNTs. The length of each CNT is 3.74 nm. Data are from the reoptimized Tersoff potential.

macroscale. The proposed packing, shown in Fig. 1(b) for a system of collapsed (30,30) CNTs, accounts for the steric effect of stacking nearly circular edges, which leads to a 49° incline of the periodicity vector in the perpendicular direction. The skewed stacking preserves the vdW contact between stacked bilayer regions (vertical direction) and between the nearly circular edges of CNTs in neighboring stacks (horizontal direction).

Using a simulation setup similar to that shown in Fig. 3, we computed κ along a skewed stack with different numbers of collapsed (30,30) CNTs. As can be seen from the results summarized in Fig. 6(b), κ becomes rapidly independent on the number of tubes, a behavior that resembles the weak layer dependence of in-plane κ in few-layer graphene [20]. Notably, the converged κ shows only a 14% reduction from the isolated collapsed (30,30) CNT.

We have also evaluated the interfacial thermal resistance R between collapsed (30,30) CNTs. To verify our method, we have first computed R across two aligned cylindrical (30,30) CNTs at their equilibrium vdW distance. R across two (30, 30) cylindrical CNTs turned out to be 2.38×10^{10} K/W, a value that is significantly larger than the 9.69×10^{9} K/W obtained in the collapsed case. The former value is in good agreement with what was obtained in previous studies [38,39] and reflects the smaller number of carbon atoms in effective vdW contact. Note that in order to avoid defining the contact area between cylindrical CNTs, here we have compared R in K/W units [38].

In spite of the good vdW contact, R between collapsed (30,30) CNTs is still large, a result that indicates that thermal transport in the stacked CNTs is strongly anisotropic. Figure 4(b) shows that R decreases with the increase in number of CNTs, and converges to 3.9×10^{-9} m^2 K/W, a value that is similar with R across few-layer graphene [40]. On the other hand, we expect that R between the nearly circular edges of collapsed CNTs in neighboring stacks to be even larger, similar to R across small-diameter cylindrical CNTs [38,39]

IV. CONCLUSION

The atomistic simulation results presented here indicate that collapsed CNTs and stacked-collapsed CNTs behave thermally like bilayers and few-layer GNRs, respectively, but free from the diffusive phonon scattering associated with rough edges and cross-plane scattering. While κ of individual collapsed CNTs can be significantly reduced by torsional deformation, the stacked collapsed bundles should be thermally robust, as the torsional rigidity of few-layer graphene ribbons increases rapidly with the number of layers [41]. Our theoretical findings are especially important in the context of the recent progress in carbon composites. In general, κ of the CNT network measures only tens of W m^{-1} K^{-1}. This is because the network structure exhibits poor alignment and low packing densities, and R at the CNT-CNT junction is viewed as a main obstacle for effective thermal transport [3]. The proposed alignment of long CNTs into stacked collapsed architectures, presents potential for processing unidirectional thermal highways in lightweight functional composite materials. The stacked architectures are further amenable to enhancing κ in the cross-plane direction by lowering the R between collapsed CNTs via polymer functionalization [42].

ACKNOWLEDGMENTS

This work was partially supported by an Early Stage Innovations grant from NASA's Space Technology Research Grants Program NNX16AE03G and by NSF CMMI Grant No. 1332228. J.A.-G. greatly acknowledges support from the Albert Swanson Fellowship. T.D. thanks the Hanse Wissenschaftskolleg Delmenhorst, Germany for hospitality. Resources supporting this work were provided by the NASA High-End Computing Program through the NASA Advanced Supercomputing Division at Ames Research Center.

[1] E. J. Siochi and J. S. Harrison, Structural nanocomposites for aerospace applications, MRS Bull. **40**, 829 (2015).

[2] Q. Cheng, B. Wang, C. Zhang, and Z. Liang, Functionalized carbon-nanotube sheet/bismaleimide nanocomposites: Mechanical and electrical performance beyond carbon-fiber composites, Small **6**, 763 (2010).

[3] T. S. Gspann, S. M. Juckes, J. F. Niven, M. B. Johnson, J. A. Elliott, M. A. White, and A. H. Windle, High thermal conductivities of carbon nanotube films and micro-fibres and their dependence on morphology, Carbon **114**, 160 (2017).

[4] S. Li, J. G. Park, Z. Liang, T. Siegrist, T. Liu, M. Zhang, Q. Cheng, B. Wang, and C. Zhang, In situ characterization of

structural changes and the fraction of aligned carbon nanotube networks produced by stretching, Carbon **50**, 3859 (2012).

[5] T. Dumitrică, M. Hua, and B. I. Yakobson, Symmetry-, time-, and temperature-dependent strength of carbon nanotubes, Proc. Natl. Acad. Sci. USA **103**, 6105 (2006).

[6] E. Pop, D. Mann, Q. Wang, K. Goodson, and H. Dai, Thermal conductance of an individual single-wall carbon nanotube above room temperature, Nano Lett. **6**, 96 (2006).

[7] Q. Cheng, J. Bao, J. G. Park, Z. Liang, C. Zhang, and B. Wang, High mechanical performance composite conductor: Multi-walled carbon nanotube sheet/bismaleimide nanocomposites, Adv. Funct. Mater. **19**, 3219 (2009).

[8] R. Downes, S. Wang, D. Haldane, A. Moench, and R. Liang, Strain-induced alignment mechanisms of carbon nanotube networks, Adv. Eng. Mater. **17**, 349 (2015).

[9] R. D. Downes, A. Hao, J. G. Park, Y.-F. Su, R. Liang, B. D. Jensen, E. J. Siochi, and K. E. Wise, Geometrically constrained self-assembly and crystal packing of flattened and aligned carbon nanotubes, Carbon **93**, 953 (2015).

[10] M. Fujii, X. Zhang, H. Xie, H. Ago, K. Takahashi, T. Ikuta, H. Abe, and T. Shimizu, Measuring the Thermal Conductivity of a Single Carbon Nanotube, Phys. Rev. Lett. **95**, 065502 (2005).

[11] J. Hone, M. Whitney, C. Piskoti, and A. Zettl, Thermal conductivity of single-walled carbon nanotubes, Phy. Rev. B **59**, R2514 (1999).

[12] J. Ma, Y. Ni, S. Volz, and T. Dumitrică, Thermal transport in single-walled carbon nanotubes under pure bending, Phys. Rev. Appl. **3**, 024014 (2015); J. Ma, Y. Ni, and T. Dumitrică, Thermal conductivity and phonon scattering in severely bent carbon nanotubes and bi-layer graphene, Mater. Today Proc. **2**, 3819 (2015).

[13] N. G. Chopra, L. X. Benedict, V. H. Crespi, and M. L. Cohen, Fully collapsed carbon nanotubes, Nature (London) **377**, 135 (1995).

[14] J. A. Elliott, J. K. W. Sandler, A. H. Windle, R. J. Young, and M. S. P. Shaffer, Collapse of Single-Wall Carbon Nanotubes Is Diameter Dependent, Phys. Rev. Lett. **92**, 095501 (2004).

[15] G. Gao, T. Çağin, and W. A. Goddard III, Energetics, structure, mechanical and vibrational properties of single-walled carbon nanotubes, Nanotechnology **9**, 184 (1998).

[16] D.-B. Zhang and T. Dumitrică, Effective strain in helical rippled carbon nanotubes: A unifying concept for understanding electromechanical response, ACS Nano **4**, 6966 (2010); Role of effective tensile strain in electromechanical response of helical graphene nanoribbons with open and closed armchair edges, Phys. Rev. B **85**, 035445 (2012).

[17] M.-H. Bae, Z. Li, Z. Aksamija, P. N. Martin, F. Xiong, Z.-Y. Ong, I. Knezevic, and E. Pop, Ballistic to diffusive crossover of heat flow in graphene ribbons, Nat. Commun. **4**, 1734 (2013).

[18] A. V. Savin, Y. S. Kivshar, and B. Hu, Suppression of thermal conductivity in graphene nanoribbons with rough edges, Phys. Rev. B **82**, 195422 (2010).

[19] S. Ghosh, W. Bao, D. L. Nika, S. Subrina, E. P. Pokatilov, C. N. Lau, and A. A. Balandin, Dimensional crossover of thermal transport in few-layer graphene, Nat. Mater. **9**, 555 (2010).

[20] W. R. Zhong, M. P. Zhang, B. Q. Ai, and D. Q. Zheng, Chirality and thickness-dependent thermal conductivity of few-layer graphene: A molecular dynamics study, Appl. Phys. Lett. **98**, 113107 (2011).

[21] H. R. Barzegar, A. Yan, S. Coh, E. Gracia-Espino, C. Ojeda-Aristizabal, G. Dunn, M. L. Cohen, S. G. Louie, T. Wågberg, and A. Zettl, Spontaneous twisting of a collapsed carbon nanotube, Nano Res. **10**, 1942 (2017).

[22] S. Plimpton, Fast parallel algorithms for short-range molecular dynamics, J. Comput. Phys. **117**, 1 (1995).

[23] T. Dumitrică and R. D. James, Objective molecular dynamics, J. Mech. Phys. Solids **55**, 2206 (2007).

[24] S. J. Stuart, A. B. Tutein, and J. A. Harrison, A reactive potential for hydrocarbons with intermolecular interactions, J. Chem. Phys. **112**, 6472 (2000).

[25] D. W. Brenner, O. A. Shenderova, J. A. Harrison, S. J. Stuart, B. Ni, and S. B. Sinnott, A second-generation reactive empirical bond order (REBO) potential energy expression for hydrocarbons, J. Phys. Condens. Matter **14**, 783 (2002).

[26] I. Nikiforov, E. Dontsova, R. D. James, and T. Dumitrică, Tight-binding theory of graphene bending, Phys. Rev. B **89**, 155437 (2014).

[27] J. Tersoff, Empirical Interatomic Potential for Carbon, with Applications to Amorphous Carbon, Phys. Rev. Lett. **61**, 2879 (1988).

[28] L. Lindsay and D. Broido, Optimized Tersoff and Brenner empirical potential parameters for lattice dynamics and phonon thermal transport in carbon nanotubes and graphene, Phys. Rev. B **81**, 205441 (2010).

[29] R. N. Salaway and L. V. Zhigilei, Molecular dynamics simulations of thermal conductivity of carbon nanotubes: Resolving the effects of computational parameters, Int. J. Heat Mass Transfer **70**, 954 (2014).

[30] See Supplemental Material at http://link.aps.org/supplemental/10.1103/PhysRevMaterials.1.056001 for κ convergence test, collapsed tube stability under MD, computed phonon dispersion, phonon density of states, and for details on the calculations of the phonon relaxation times.

[31] A. Cao and J. Qu, Size dependent thermal conductivity of single-walled carbon nanotubes, J. Appl. Phys. **112**, 013503 (2012).

[32] J. R. Lukes and H. Zhong, Thermal conductivity of individual single-wall carbon nanotubes, J. Heat Transfer **129**, 705 (2007).

[33] N. Mingo and D. A. Broido, Carbon Nanotube Ballistic Thermal Conductance and Its Limits, Phys. Rev. Lett. **95**, 096105 (2005).

[34] J. Wang and J.-S. Wang, Carbon nanotube thermal transport: ballistic to diffusive, Appl. Phys. Lett. **88**, 111909 (2006).

[35] T. Zhu and E. Ertekin, Resolving anomalous strain effects on two-dimensional phonon flows: The cases of graphene, boron nitride, and planar superlattices, Phys. Rev. B **91**, 205429 (2015).

[36] T. Feng, B. Qiu, and X. Ruan, Anharmonicity and necessity of phonon eigenvectors in the phonon normal mode analysis, J. Appl. Phys. **117**, 195102 (2015).

[37] J. A. Thomas, J. E. Turney, R. M. Iutzi, C. H. Amon, and A. J. McGaughey, Predicting phonon dispersion relations and lifetimes from the spectral energy density, Phys. Rev. B **81**, 081411 (2010).

[38] C.-J. Hu and B.-Y. Cao, Thermal resistance between crossed carbon nanotubes: Molecular dynamics simulations and analytical modeling, J. Appl. Phys. **114**, 224308 (2013).

[39] V. Varshney, S. S. Patnaik, A. K. Roy, and B. L. Farmer, Modeling of thermal conductance at transverse CNT–CNT interfaces, J. Phys. Chem. C **114**, 16223 (2010).

[40] Y. Ni, Y. Chalopin, and S. Volz, Significant thickness dependence of the thermal resistance between

few-layer graphenes, Appl. Phys. Lett. **103**, 061906 (2013).

[41] E. Dontsova and T. Dumitrică, Nanomechanics of twisted mono- and few-layer graphene nanoribbons, J. Phys. Chem. Lett. **4**, 2010 (2013).

[42] Y. Ni, H. Han, S. Volz, and T. Dumitrică, Nanoscale azide polymer functionalization: a robust solution for suppressing the carbon nanotube–polymer matrix thermal interface resistance, J. Phys. Chem. C **119**, 12193 (2015).